







Direct spectral measurements of midinfrared radiation from a laser wakefield acceleratorA. E. Hussein ^{1,2,*}, J. D. Ludwig,³ Y. Ma ¹, P.-E. Masson-Laborde ^{4,5}, P. J. Skrodzki,¹ J. Hinojosa,¹ E. Peterson ¹, I. Jovanovic ¹, A. Maksimchuk ¹, J. Nees,¹ A. G. R. Thomas,¹ W. Rozmus,³ and K. Krushelnick¹¹*Gérard Mourou Center for Ultrafast Optical Science, University of Michigan, Ann Arbor, Michigan 48109, USA*²*Department of Electrical and Computer Engineering, University of Alberta, Edmonton, Alberta, T6G 2J1, Canada*³*Department of Physics, University of Alberta, Edmonton, Alberta, T6G 2J1, Canada*⁴*CEA, DAM, DIF, F-91297 Arpajon, France*⁵*Université Paris-Saclay, CEA, LMCE, 91680 Bruyères-le-Châtel, France*

(Received 1 October 2022; accepted 3 November 2022; published 8 December 2022)

The formation of plasma waves during laser wakefield acceleration (LWFA) produces time-dependent frequency shifts in the driving laser pulse, extending its spectral content to the infrared. We present direct spectral measurements of multi-mJ infrared pulses from an LWFA. Experimental beam profile measurements and three-dimensional particle-in-cell simulations suggest high focusability of these pulses. Particle-in-cell simulations demonstrate that the measurement of side-scattered infrared radiation may serve as a diagnostic of plasma waves and the efficiency of spectral broadening during LWFA.

DOI: [10.1103/PhysRevA.106.063505](https://doi.org/10.1103/PhysRevA.106.063505)**I. INTRODUCTION**

The infrared (IR) spectral region of 2–20 μm contains the frequency range of molecular vibrations and is of significant interest for a range of scientific and technological applications [1–4]. Intense IR pulses have exciting applications in attosecond science [5], high-harmonic generation [6,7], high-field physics [8,9], and laser-plasma accelerators [10–12] due to the scaling of the ponderomotive energy as $U_p \propto I\lambda^2$. Optical parametric amplifiers, frequency combs, and fiber lasers have yielded intense, few-cycle infrared pulses [13–22]. However, the generation of wavelength-tunable infrared pulses, optimized for power, efficiency, and spectral performance, is particularly challenging. The use of a plasma medium to extend the spectral content of laser pulses into the infrared through nonlinear self-phase modulation provides an avenue for the controlled production of such pulses that is scalable to relativistic intensities [23].

Plasma waves have been shown to produce an upshift (or downshift) of the driving laser frequency due to a time-varying refractive index, resulting in photon acceleration (or deceleration), pulse compression, and the generation of wavelengths extending to IR [24–32]. According to one-dimensional (1D) nonlinear theory [33], for relativistic laser intensities ($a_0 > 1$), the refractive index seen by the laser is $\eta \simeq 1 - \frac{\omega_p^2}{2\omega_0^2} \frac{1}{1+\phi}$ for $\omega_p \ll \omega_0$, where ω_0 is the laser frequency, $\omega_p = \sqrt{4\pi n_e e^2/m_e}$ is the plasma frequency, and ϕ is the normalized scalar potential. A copropagating gradient in η due to density gradients in the plasma will lead to variations in the laser's spectral content through a combination of asymmetric self-phase modulation and group-velocity dispersion.

Plasma waves formed during laser wakefield acceleration (LWFA) [34,35] can result in an asymmetric shifting of the laser spectrum. In the “bubble” regime of LWFA [36–38], a copropagating density up-ramp at the leading edge of the plasma bubble creates a negative refractive index gradient, causing a frequency downshift of the laser pulse. The back of the wakefield bubble has a positive refractive index gradient; light in this region is frequency upshifted. When the pulse duration is on the order of the plasma wavelength, the body of the pulse will reside in a region of falling electron density, and redshifting will dominate the spectral evolution, producing wavelengths extending into the IR regime. The first experimental realization of LWFA mid-IR pulses was reported by Pai *et al.* [39], with pulses within the spectral range of 2–20 μm containing ~ 3 mJ of energy. Recent computational and experimental work [23,40,41] has demonstrated that tunable, single-cycle pulses with wavelengths extending to 20 μm may be achieved using tailored density plasma targets.

Here, we present high-resolution spectral measurements of IR pulses from an LWFA, extending to 2.5 μm and containing up to 15 mJ of energy in the 1–9 μm range (conversion efficiency of $\simeq 0.64\%$). Experimental measurements of the near-field and three-dimensional (3D) simulations suggest high focusability, highlighting the capabilities of LWFA for the generation of intense mid-IR sources. Tailored density plasma targets were found to play a significant role in spectral broadening, and under certain conditions narrow spectral features were produced, suggesting the potential for control of IR radiation using adaptive control and/or machine learning techniques. Accordingly, a statistical analysis of long-wavelength generation and pulse energy was performed to examine the correlation of laser and plasma parameters with the spectral features and energy content of IR pulses. 3D simulations demonstrate that slow-moving, long-wavelength light can interact with the negative density gradient at the back

*aehussein@ualberta.ca

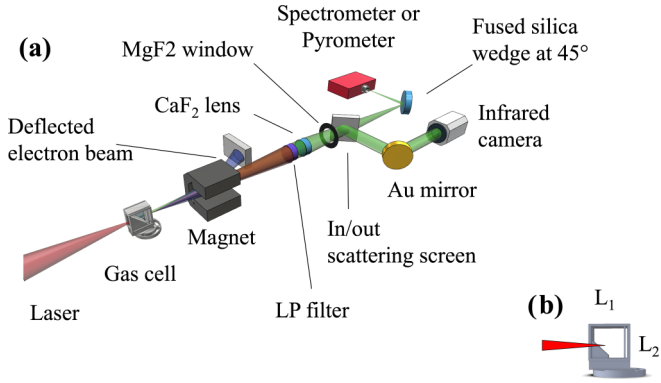


FIG. 1. (a) Experimental setup for measurement of transmitted LWFA-generated infrared radiation. (b) Two-stage gas cell, with a 5–20 mm variable length first stage L_1 and a 1 mm fixed length second stage L_2 .

of the wakefield bubble(s), resulting in blueshifting and side scattering of mid-IR pulses that may serve as a diagnostic of plasma waves as well as the efficiency of spectral broadening during LWFA.

II. EXPERIMENTAL SETUP

Experiments were conducted using the HERCULES Ti:sapphire laser system at the University of Michigan [42]. The laser beam had a full width at half maximum (FWHM) pulse duration of (35 ± 3) fs and was focused using an $f/20$ off-axis parabolic mirror to a focal spot of $26 \pm 0.8 \mu\text{m}$ ($1/e^2$). The average power after compression varied from 40 ± 6 to 77 ± 8 TW, corresponding to laser intensities of 3.9×10^{18} – 7.2×10^{18} W/cm². The experimental setup is presented in Fig. 1(a) with details of two-stage cells in Fig. 1(b).

Two types of 3D printed gas cells [43] were used to produce low-density plasma targets: a 5–20 mm variable length cell, and a 5–20 mm two-stage gas cell with a 1-mm rear compartment [44]. The plasma density was controlled by altering the pressure of the gas supply, containing 98% helium and 2% nitrogen gas; each cell compartment was connected to an independent mixed gas source. As the laser traveled through the gas, it drove an LWFA [34], with the ponderomotive expulsion of electrons creating an ion cavity in its wake. A dipole magnet (0.8 T, 15 cm long) was used to deflect the resultant electron beam onto a Lanex scintillating screen imaged by a CCD camera. Density measurements were made using a shearing Michelson interferometer, yielding maximum plasma densities up to 1.3×10^{19} cm⁻³ in the main stage. The density in the second stage cell of 1 mm length was estimated by scaling interferometry measurements by the ratio of the volumes between the stages using the ideal gas equation.

Transmitted radiation passed through a 1050-nm long-pass (LP) filter and a CaF₂ lens ($f = 50$ cm) before exiting the chamber via a MgF₂ window to all beam diagnostics. For CaF₂ and MgF₂, optical transmission drops to less than 20% for $\lambda > 9.5 \mu\text{m}$, therefore we consider the range of energy measurements to be approximately 1–9 μm . High-resolution spectral measurements were made using a NIRQuest512-2.5 spectrometer (75 line pairs/mm grating, 25 μm entrance slit,

1.0 ms integration time) measuring 900–2500 nm light. Light entering the spectrometer was reflected from a fused silica wedge at 45°. Spectra were background subtracted and corrected for detector efficiency and losses due to all optical elements. A low-pass filter was applied to experimental and simulation spectra to remove high-frequency noise. The energy in the IR pulse was measured using a calibrated hybrid pyrometric detector (QS3-IL) interchanged with the spectrometer. The quoted energy values are background subtracted and account for the solid angle and transmission through all optical elements. For beam profile measurements, a scattering screen was placed at the exit of the chamber window and imaged using a Xenics Onca-MWIR-InSb camera, measuring 1–5 μm . A median noise filter was applied to the beam profile images for noise reduction.

III. PARTICLE-IN-CELL SIMULATIONS

To understand the experimental results, two- and three-dimensional particle-in-cell (PIC) simulations were performed in a moving frame using the fully relativistic OSIRIS 4.0 framework [45,46]. An 800 nm, 30 fs, $f/20$, Gaussian laser pulse with 30–60 TW power was simulated. The pulse was linearly polarized in \hat{z} (transverse to the simulation domain) and entered the middle of the box at $y = 100 \mu\text{m}$. Single- and two-stage density profiles were simulated, with varying electron densities in the main stage ($n_{e,1}$, $L_1 = 5$ –10 mm) and second stage ($n_{e,2}$, $L_2 = 1$ mm), where present. The electron temperature was initialized to $T_e = 10$ eV. For 2D simulations, the simulation box was $200 \times 200 \mu\text{m}$ with stationary ions, 50 cells/ μm resolution, and 20 electron particles per cell. 3D PIC simulations were performed for validation and further insight into the process with a reduced resolution of $6000 \times 1500 \times 1500$ and 2 electron particles per cell. A two-stage gas cell with $n_{e,1} = 4 \times 10^{18}$ cm⁻³, $L_1 = 10$ mm, $n_{e,2} = 1.2 \times 10^{19}$ cm⁻³, and $L_2 = 1$ mm was simulated.

IV. RESULTS AND ANALYSIS

In experimental measurements, spectral broadening was consistently limited to below 2 μm using a single-stage cell [Fig. 2(a)]. However, density tailoring using the second stage had a profound impact on spectral broadening, producing wavelengths extending to the detector limit [Fig. 2(b)]. All presented spectra are averaged from at least three shots at identical experimental conditions. For the single stage ($L_1 = 5$ mm, $P = 40 \pm 6$ TW), the plasma density $n_{e,1}$ was varied from 4.2×10^{18} to 1.1×10^{19} cm⁻³. The two-stage gas cell had a density of $n_{e,1} = 4.2 \times 10^{18}$ cm⁻³ in the main (long) stage ($L_1 = 9$ mm, $L_2 = 1$ mm, $P = 50 \pm 3$ TW), while the density in the secondary stage, $n_{e,2}$ ($L_2 = 1$ mm), was varied from 8.3×10^{18} to 3.3×10^{19} cm⁻³.

In the two-stage cell, the greatest spectral broadening was achieved with $n_{e,2} = 2.2 \times 10^{19}$ cm⁻³ [Fig. 2(b)], but decreased with increasing density. This is because at high density, the wakefield bubble may shrink or break into several bubbles, no longer containing the long wavelengths. Additionally, a reduction in signal intensity at the highest densities was observed with both target types, and is attributed to the

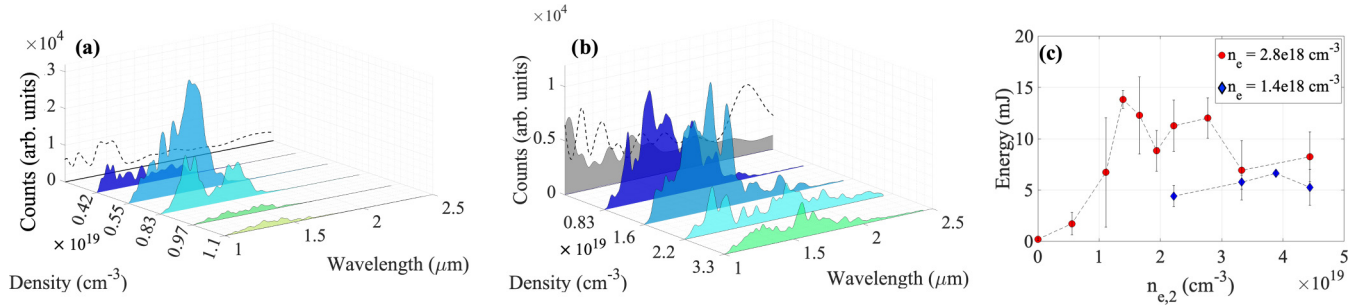


FIG. 2. Spectral lineouts of the exiting mid-IR pulse from different gas cells. (a) Single-stage gas cell with varied density $n_{e,1}$. (b) Two-stage gas cell with $n_{e,1} = 4.2 \times 10^{18} \text{ cm}^{-3}$ and varied $n_{e,2}$. 2D (3D) PIC spectra are shown as a dashed line (gray area) on the zero-density plane. (c) Mid-IR energy as a function of $n_{e,2}$.

collapse of the bubble cavity and attenuation of escaping radiation in the plasma. Prior to the onset of signal attenuation due to increased plasma density, spectral broadening was found to increase with plasma density due to the associated drop in the critical power for self-focusing, which enhances the ponderomotive force, creating greater charge displacement and a steeper refractive index gradient. The longest average wavelength of $\lambda \simeq 1.55 \mu\text{m}$ was obtained with a ratio of approximately 4 between the main and second stages ($n_{e,1} = 4.2 \times 10^{18} \text{ cm}^{-3}$, $n_{e,2} = 1.7 \times 10^{19} \text{ cm}^{-3}$).

Enhanced spectral broadening with density-tailored targets is consistent with PIC simulations as well as recent experimental and computational work [23,40]. Lineouts of the laser field at $y = 100 \mu\text{m}$ from PIC simulations were Fourier transformed after the light exited the plasma at $t \simeq 40 \text{ ps}$. Experimental spectral features are compared with 2D and 3D simulations in the zero-density plane of Figs. 2(a) and 2(b) as a dashed line and gray shaded area, respectively. 2D simulations were performed for a single-density stage with $n_{e,1} = 2.0 \times 10^{18} \text{ cm}^{-3}$, $L_1 = 5 \text{ mm}$, and a two-stage with $n_{e,1} = 4.0 \times 10^{18} \text{ cm}^{-3}$, $L_1 = 5 \text{ mm}$, $n_{e,2} = 1.2 \times 10^{19} \text{ cm}^{-3}$, $L_2 = 1 \text{ mm}$. 3D results in Fig. 2(b) reasonably reproduce experimental features. 2D PIC simulations showed a higher rate of redshifting than observed in experiments and 3D simulations which are attributed to an underestimation of the effect of diffraction.

Mid-IR pulses measured in experiments contained energy up to $(15.3 \pm 3.0) \text{ mJ}$ (conversion efficiency of $\simeq 0.64\%$) in the range of 1–9 μm [Fig. 2(c)]. The total energy in the mid-IR pulse initially increased with density in the second stage due to the requirement of steep density gradients for optimized spectral broadening. However, the total energy later plateaued and eventually decayed due to the attenuation of long-wavelength light in high-density plasma.

Experimental near-field measurements of the mid-IR beam demonstrate good spatial uniformity in the range of 1–5 μm [Fig. 3(a)], obtained at $P = 77 \pm 8 \text{ TW}$, $n_{e,1} = 2.8 \times 10^{18} \text{ cm}^{-3}$, $L_1 = 6 \text{ mm}$, $n_{e,2} = 2.2 \times 10^{18} \text{ cm}^{-3}$, $L_2 = 1 \text{ mm}$. Uniform beam profiles may indicate that the plasma bubble serves as a spatial filter for long wavelengths and that the process is capable of producing pulses with good focusability; pulses were successfully focused using a MgF_2 lens to ablate the surface of a copper sample with a single shot. In the 3D simulation, the laser electric field (E_z) component was squared and integrated along the propagation direction to

obtain the simulated focal spot shown in Fig. 3(b) including the full laser spectrum, with a FWHM of approximately 5 μm .

Another important consideration for the applicability of these sources is shot-to-shot variations. Figure 4(a) presents spectra measured at nominally identical experimental conditions, with low density in the first stage, followed by a density ramp: $n_{e,1} = 2.8 \times 10^{18} \text{ cm}^{-3}$, $n_{e,2} = 1.7 \times 10^{19} \text{ cm}^{-3}$, $P = (71 \pm 3) \text{ TW}$. In three shots at these conditions, narrow spectra with a central wavelength of $\lambda \simeq 1.4 \mu\text{m}$ and a FWHM spectral spread of $\Delta\lambda \sim 100 \text{ nm}$ were measured [Fig. 4(a), shots 6–8]. However, pulses spanning nearly the full detector range as well as highly attenuated pulses were also measured at these conditions [Fig. 4(a), shots 1–5]. The corresponding electron beams are shown in Fig. 4(b). Narrow spectral features ($\Delta\lambda \sim 100 \text{ nm}$) were associated with reduced beam charge ($Q = 23.1 \pm 10.6 \text{ pC}$) as compared to broadened or attenuated pulses ($Q = 38.9 \pm 25.3 \text{ pC}$).

To investigate the correlation between laser, plasma, and electron beam parameters and spectral broadening, the covariance of these parameters with the fraction of radiation from 2 to 2.5 μm and the total energy in the mid-IR pulse was calculated using data from two-stage cells. Nine parameters were considered: (1) laser power (P), (2) pulse duration (t_p), (3) plasma length (L), (4) density in the main stage ($n_{e,1}$), (5) density in the second stage ($n_{e,2}$), (6) density ratio ($n_{e,2}/n_{e,1}$), (7) total charge in the accelerated beam (Q), (8) electron beam divergence (θ), and (9) maximum beam energy (ϵ_{max}). Data from 225 shots were used to study variation with spectral broadening, and from 88 shots for pulse energy. In general,

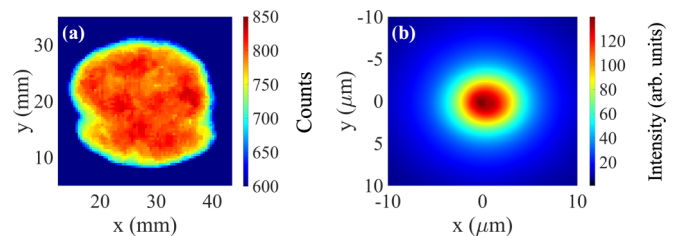


FIG. 3. (a) Experimental near-field beam profile of 1–5 μm light. (b) Focal spot produced using the full spectrum of light from the 3D PIC simulation.

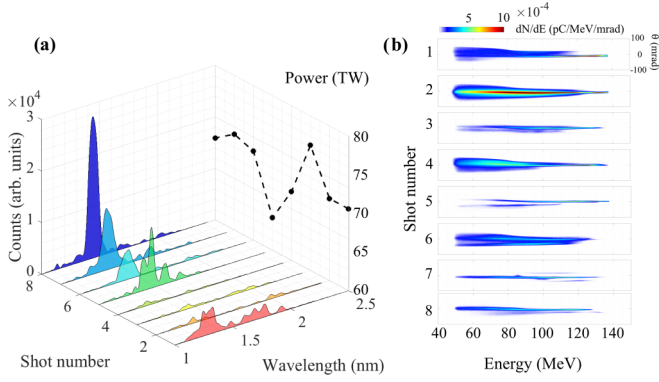


FIG. 4. (a) Shot-to-shot variations of the spectra of the exiting mid-IR pulse and laser power over 8 shots. (b) Corresponding electron spectra for each shot shown in (a).

the sample covariance matrix of a matrix X is given by

$$\Sigma(X) = \frac{1}{n}XX^T - \mu_X\mu_X^T, \quad (1)$$

where $\mu_X = (1/n)X$ is the mean column vector of X . The resultant matrix $\Sigma(X)$ is of size $(m+1) \times (m+1)$, where the diagonal elements are the covariance of a variable with itself. The covariance of each parameter (m) with respect to the variable of interest, (a, b), is contained in the final row of $\Sigma_{(a,b)}(X)$, in which a value of zero indicates no covariance. The Pearson correlation coefficient ρ , a measure of the linear correlation between variables yielding $\rho \in [-1, 1]$, is then calculated using $\Sigma(X)$. This coefficient is a measure of the linear correlation between variables, yielding $\rho \in [-1, 1]$, with $+1$ (-1) indicating positive (negative) linear correlation. A value of zero indicates no correlation. In general, Pearson's correlation coefficient for two variables x and y is

$$\rho_{x,y} = \frac{\Sigma(x,y)}{\sigma_x\sigma_y}, \quad (2)$$

where σ is the standard deviation. From the covariance matrix $\Sigma(X)$, σ is the square root of the diagonal.

From this analysis, the plasma length and density in the first stage were found to have the strongest correlation, ρ_a , with the production of wavelengths extending from 2

TABLE I. Pearson correlation coefficients calculated from two covariance matrices formed by nine parameters, where ρ_a is the fraction of radiation with wavelengths between 2 and 2.5 μm and ρ_b is the total energy in the spectrally broadened pulse.

Parameter (m)	ρ_a	ρ_b
P	0.85	0.78
t_p	0.49	0.44
L_1	0.96	0.68
$n_{e,1}$	0.88	0.76
$n_{e,2}$	0.63	0.84
$n_{e,2}/n_{e,1}$	0.85	0.66
Q	0.70	0.63
θ	0.11	0.23
ϵ_{max}	0.61	0.54

to 2.5 μm [$\rho_a(L) = 0.96$, $\rho_a(n_{e,1}) = 0.87$]. The energy in the mid-IR pulse had the strongest correlation, ρ_b , with the density in the second stage and laser power [$\rho_b(n_{e,2}) = 0.84$, $\rho_b(P) = 0.78$]. These results indicate that spectral broadening from an LWFA is highly dependent on fluctuations in multiple variables. The optimization of mid-IR pulses from an LWFA would be best conducted using high-repetition rate laser systems, where adaptive control methods, such as those in Refs. [11,47,48], could be applied to converge on ideal conditions. Of the electron beam properties investigated, beam charge was found to have the highest correlation with spectral broadening and pulse energy, with $\rho_a(Q) = 0.70$ and $\rho_b(Q) = 0.63$, respectively. Pearson coefficients of all parameters are presented in Table I.

A detailed analysis of 3D PIC simulations shows that the long-wavelength light generated during LWFA slips backward relative to the driving laser due to its slower group velocity [Fig. 5(a)]. Initially, this results in power amplification [49,50] as the pulse becomes compressed. However, as the receding IR pulse lags further behind, it approaches the negative density gradient corresponding to the back of the first bubble [Fig. 5(b)]. In time, if the IR pulse is not released from its bubble “container” into vacuum (i.e., exits the plasma), the spectrum will continue to broaden, blueshifting as it approaches the back of the bubble. With sufficient

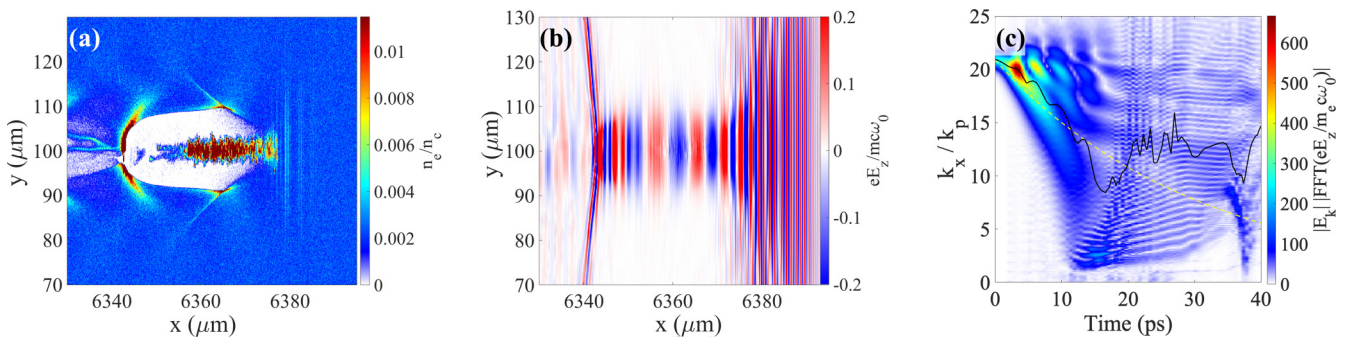


FIG. 5. Snapshots from 3D PIC simulations at $t = 20.7$ ps in a frame moving at the speed of light. (a) The plasma electron density and accelerated bunch within the bubble. (b) The laser field E_z , saturated to focus on receding long-wavelength light. (c) Temporal evolution of the axial electromagnetic spectrum in wave number ($k \propto 1/\lambda$). The solid black line corresponds to the mean wave number from the simulation spectrum; the dashed yellow line corresponds to a theoretical mean wave number calculated from Ref. [53]. Note that light exits the plasma at approximately 40 ps.

ponderomotive force, IR light can break through the back of this first bubble and extend into subsequent bubbles. However, as the efficiency drops, the ponderomotive force of the spectrally broadened light also reduces, until it is no longer able to break through the back of the bubble and will instead side scatter. Here, the swallowtail catastrophe [51] occurs due to particles emerging from the sides of the bubble as it propagates forward. Simulations reveal that the pulse is blueshifted and side scattered from the laser axis by density perturbations of the swallowtail cone behind the first bubble [$x = 6340 \mu\text{m}$ in Fig. 5(b)]. At this point, side-scattered light has a field amplitude of 0.26, compared to 0.2 to pulse at the center of the bubble, indicating that side-scattered light is sufficiently intense to be used as a diagnostic of reduced efficiency into spectral broadening.

Lineouts of the laser field E_z at $y = 100 \mu\text{m}$ were Fourier transformed to show the time history of the spectral content of the laser pulse [Fig. 5(c); note that $\lambda \propto 1/k$]. As the long-wavelength light lags behind the driving pulse and passes through the wake, it is modulated on the scale of the plasma wavelength $\sim 1/k_p$ [52], as shown at $t > 10$ ps. A theoretical estimate [53] of the mean wave number $\langle k \rangle$ assumes redshifting at a characteristic length scale of the pump depletion length $L_{\text{pd}} \approx 8.7k_0^2/k_p^3$, from conservation of energy and wave action, and is independent of laser amplitude for $a_0 \gg 1$. This can be expressed as $\langle k(t) \rangle = \langle k(0) \rangle e^{-ct/L_{\text{pd}}}$. The simulated and theoretical values of the mean wave number as a function of time are plotted in Fig. 5(c) in solid black and dashed yellow lines, respectively. The theoretical curve shows good agreement with simulations during the time in which the receding light does not interact with the wake ($t < 15$ ps). However, once the receding light interacts with the backs of the wakefield bubbles it gains spectral components associated with k_p , and the pulse undergoes blueshifting and a reduction in intensity.

The spectral content and pulse duration of the shifted light could be controlled by varying the bubble size (plasma density). The plasma length can also be tailored to terminate the process once the first bubble has been filled, letting IR light exit the bubble and the plasma before the onset of blueshifting at the back of the wakefield bubble. Given the extent of the spectral broadening, and the size of the bubble, IR light can approach single cycle for a given wavelength [40] (i.e. $10 \mu\text{m}$ light in a $10 \mu\text{m}$ bubble). Using a longer plasma, the pulse duration near the end of the plasma in 3D simulations is approximately 100 fs and the average wavelength corresponds to $k/k_p \simeq 12.5$ [Fig. 5(c)]. Through tailoring of the plasma density and monitoring of side-scattered IR radiation the duration of the laser pulse could be optimized for shortest duration at a given wavelength.

Long-wavelength light may also affect the properties of the accelerated electron bunch through interaction with the back of the wakefield bubble, causing sheath deformation. The interaction of the long-wavelength light with the electron beam in the bubble also increases the transverse emittance of the electron bunch along the laser polarization direction [29,54–56]; these are important considerations for the use of plasma wakefields for accelerator applications and could be further studied through measurement of IR side scattering.

Finally, simulations indicate that the narrow spectral features observed in Fig. 4(a) likely correspond to one of the spectral branches in Fig. 5(c) escaping the plasma before undergoing significant modulation due to an interaction with the wakefield bubbles. Both PIC simulations and theory suggest that the rate of redshifting is reduced at low plasma density. This is particularly relevant when the bursting into long-wavelengths occurs at the leading edge of the bubble [$t \approx 10$ ps in Fig. 5(c)]. In low-density plasma, the rate of redshifting may be slowed such that there is more tolerance to the variations in plasma conditions. The interaction and evanescence of IR light propagating through plasma is also reduced at low density, and the corresponding extension in plasma wavelength (i.e., bubble size) provides more space between redshifting at the front of the bubble and blueshifting at the rear, reducing the detrimental effects of pulse interaction with the back of the bubble structure, and allowing for more IR light to escape.

V. SUMMARY

We have demonstrated the experimental implementation of density-tailored targets for the production of multi-mJ mid-IR pulses from an LWFA. Direct spectral measurements enabled examination of spectral features in the mid-IR range of 1–2.5 μm and beam profile measurements of IR pulses were obtained. Pulses were measured to contain up to 15 mJ of energy in the range of 1–9 μm . IR pulses generated via LWFA are unique and highly versatile in that they are simultaneously produced and inherently synchronized with energetic electrons beams [57,58] and hard x-ray sources [59,60], a crucial step in the advancement of LWFA as a multimodal alternative accelerator technology. Further, the generation of narrow IR spectra and statistical analysis of the correlation of spectral features with variations in laser, plasma, and electron beam properties indicate that the conditions necessary for control of a spectral broadening may be achieved using feedback, adaptive control, and/or machine learning techniques [47] with high-repetition rate laser systems. Supporting PIC simulations reveal that slow-moving IR light can interact with the backs of the wakefield bubble(s), resulting in blueshifting and side scattering that may serve as a diagnostic of bubble formation and a tool for optimizing the conversion efficiency into IR pulses.

ACKNOWLEDGMENTS

We acknowledge support from the Air Force Office of Scientific Research (Grant No. FA9550-16-1-0121), the Department of Energy (Grant No. DE-SC0020070), the National Science Foundation (Grant No. 1804463), the National Science and Engineering Research Council of Canada (PGSD3-471602-2015), and the University of California President's Postdoctoral Fellowship program. The authors acknowledge Compute Canada for computational resources, and the OSIRIS consortium (UCLA/IST) for use of the OSIRIS 4.0 framework. We also thank Prof. S. Rand, L. Chen, and X. Xiao for their loan of experimental equipment, and Prof. Frankling Dollar for enlightening discussions about infrared sources.

- [1] R. M. Hochstrasser, Two-dimensional spectroscopy at infrared and optical frequencies, *Proc. Natl. Acad. Sci. U.S.A.* **104**, 14190 (2007).
- [2] D. Jung, S. Bank, M. L. Lee, and D. Wasserman, Next-generation mid-infrared sources, *J. Opt.* **19**, 123001 (2017).
- [3] A. Hoffman, Extending opportunities, *Nat. Photonics* **6**, 407 (2012).
- [4] D. Woodbury, R. M. Schwartz, E. Rockafellow, J. K. Wahlstrand, and H. M. Milchberg, Absolute Measurement of Laser Ionization Yield in Atmospheric Pressure Range Gases over 14 Decades, *Phys. Rev. Lett.* **124**, 013201 (2020).
- [5] C. Hernández-García, J. A. Pérez-Hernández, T. Popmintchev, M. M. Murnane, H. C. Kapteyn, A. Jaron-Becker, A. Becker, and L. Plaja, Zeptosecond High Harmonic keV X-Ray Waveforms Driven by Midinfrared Laser Pulses, *Phys. Rev. Lett.* **111**, 033002 (2013).
- [6] T. Popmintchev, M.-C. Chen, A. Bahabad, M. Gerrity, P. Sidorenko, O. Cohen, I. P. Christov, M. M. Murnane, and H. C. Kapteyn, Phase matching of high harmonic generation in the soft and hard x-ray regions of the spectrum, *Proc. Natl. Acad. Sci. U.S.A.* **106**, 10516 (2009).
- [7] T. Popmintchev, M.-C. Chen, D. Popmintchev, P. Arpin, S. Brown, S. Ališauskas, G. Andriukaitis, T. Balčiūnas, O. D. Mücke, A. Pugžlys *et al.*, Bright coherent ultrahigh harmonics in the keV x-ray regime from mid-infrared femtosecond lasers, *Science* **336**, 1287 (2012).
- [8] P. Colosimo, G. Doumy, C. I. Blaga, J. Wheeler, C. Hauri, F. Catoire, J. Tate, R. Chirila, A. M. March, G. G. Paulus *et al.*, Scaling strong-field interactions towards the classical limit, *Nat. Phys.* **4**, 386 (2008).
- [9] B. Wolter, M. G. Pullen, M. Baudisch, M. Sclafani, M. Hemmer, A. Senftleben, C. D. Schröter, J. Ullrich, R. Moshhammer, and J. Biegert, Strong-Field Physics with Mid-IR Fields, *Phys. Rev. X* **5**, 021034 (2015).
- [10] D. Papp, J. C. Wood, V. Gruson, M. Bionta, J. N. Gruse, E. Cormier, Z. Najmudin, F. Légaré, and C. Kamperidis, Laser wakefield acceleration with high-power, few-cycle mid-IR lasers, *Nucl. Instrum. Methods Phys. Res., Sect. A* **909**, 145 (2018).
- [11] J. Lin, Y. Ma, R. Schwartz, D. Woodbury, J. A. Nees, M. Mathis, A. G. R. Thomas, K. Krushelnick, and H. Milchberg, Adaptive control of laser-wakefield accelerators driven by mid-IR laser pulses, *Opt. Express* **27**, 10912 (2019).
- [12] D. Woodbury, L. Feder, V. Shumakova, C. Gollner, R. Schwartz, B. Miao, F. Salehi, A. Korolov, A. Pugžlys, A. Baltuška, and H. M. Milchberg, Laser wakefield acceleration with mid-IR laser pulses, *Opt. Lett.* **43**, 1131 (2018).
- [13] O. D. Mücke, S. Ališauskas, A. J. Verhoef, A. Pugžlys, A. Baltuška, V. Smilgevičius, J. Pocius, L. Giniūnas, R. Danielius, and N. Forget, Self-compression of millijoule 1.5 μm pulses, *Opt. Lett.* **34**, 2498 (2009).
- [14] G. Andriukaitis, T. Balčiūnas, S. Ališauskas, A. Pugžlys, A. Baltuška, T. Popmintchev, M.-C. Chen, M. M. Murnane, and H. C. Kapteyn, 90 GW peak power few-cycle mid-infrared pulses from an optical parametric amplifier, *Opt. Lett.* **36**, 2755 (2011).
- [15] A. Schliesser, N. Picqué, and T. W. Hänsch, Mid-infrared frequency combs, *Nat. Photonics* **6**, 440 (2012).
- [16] S. Duval, M. Bernier, V. Fortin, J. Genest, M. Piché, and R. Vallée, Femtosecond fiber lasers reach the mid-infrared, *Optica* **2**, 623 (2015).
- [17] G. Fan, T. Balčiūnas, T. Kanai, F. Flöry, G. Andriukaitis, B. E. Schmidt, F. Légaré, and A. Baltuška, Hollow-core-waveguide compression of multi-millijoule CEP-stable 3.2 μm pulses, *Optica* **3**, 1308 (2016).
- [18] S. Wandel, M.-W. Lin, Y. Yin, G. Xu, and I. Jovanovic, Parametric generation and characterization of femtosecond mid-infrared pulses in ZnGeP₂, *Opt. Express* **24**, 5287 (2016).
- [19] V. Shumakova, P. Malevich, S. Ališauskas, A. Zheltikov, D. Faccio, D. Kartashov, A. Baltuška, and A. Pugžlys, Terawatt-level few-cycle mid-IR pulses through nonlinear self-compression in bulk, [arXiv:1506.01226](https://arxiv.org/abs/1506.01226).
- [20] V. Shumakova, P. Malevich, S. Ališauskas, A. Voronin, A. M. Zheltikov, D. Faccio, D. Kartashov, A. Baltuška, and A. Pugžlys, Multi-millijoule few-cycle mid-infrared pulses through nonlinear self-compression in bulk, *Nat. Commun.* **7**, 12877 (2016).
- [21] X. Xiao, J. A. Nees, and I. Jovanovic, High-energy nanosecond parametric source at 2.7 μm , *Appl. Opt.* **60**, 3585 (2021).
- [22] Y. Pertot, N. Thiré, R. Maksimenka, O. Albert, and N. Forget, 100 kHz tunable mid-IR ultrafast sources for high intensity applications, in *Emerging Laser Technologies for High-Power and Ultrafast Science*, edited by F. Légaré (IOP, Bristol, UK, 2021), pp. 4-1 to 4-22.
- [23] Z. Nie, C.-H. Pai, J. Hua, C. Zhang, Y. Wu, Y. Wan, F. Li, J. Zhang, Z. Cheng, Q. Su, S. Liu, Y. Ma, X. Ning, Y. He, W. Lu, H.-H. Chu, J. Wang, W. B. Mori, and C. Joshi, Relativistic single-cycle tunable infrared pulses generated from a tailored plasma density structure, *Nat. Photonics* **12**, 489 (2018).
- [24] S. C. Wilks, J. M. Dawson, W. B. Mori, T. Katsouleas, and M. E. Jones, Photon Accelerator, *Phys. Rev. Lett.* **62**, 2600 (1989).
- [25] E. Esarey, A. Ting, and P. Sprangle, Frequency shifts induced in laser pulses by plasma waves, *Phys. Rev. A* **42**, 3526 (1990).
- [26] C. D. Murphy, R. M. G. M. Trines, J. Vieira, A. J. W. Reitsma, R. Bingham, J. L. Collier, E. J. Divall, P. S. Foster, C. J. Hooker, A. J. Langley, P. A. Norreys, R. A. Fonseca, F. Fiuza, L. O. Silva, J. T. Mendoca, W. B. Mori, J. G. Gallacher, R. Viskup, D. A. Jaroszynski, S. P. D. Mangles *et al.*, Evidence of photon acceleration by laser wake fields, *Phys. Plasmas* **13**, 033108 (2006).
- [27] F. S. Tsung, C. Ren, L. O. Silva, W. B. Mori, and T. Katsouleas, Generation of ultra-intense single-cycle laser pulses by using photon deceleration, *Proc. Natl. Acad. Sci. U.S.A.* **99**, 29 (2002).
- [28] D. F. Gordon, B. Hafizi, R. F. Hubbard, J. R. Penano, P. Sprangle, and A. Ting, Asymmetric Self-Phase Modulation and Compression of Short Laser Pulses in Plasma Channels, *Phys. Rev. Lett.* **90**, 215001 (2003).
- [29] W. Zhu, J. P. Palastro, and T. M. Antonsen, Pulsed mid-infrared radiation from spectral broadening in laser wakefield simulations, *Phys. Plasmas* **20**, 073103 (2013).
- [30] J. D. Ludwig, P.-E. Masson-Laborde, S. Hüller, W. Rozmus, and S. C. Wilks, Enhancement and control of laser wakefields via a backward raman amplifier, *Phys. Plasmas* **25**, 053108 (2018).

- [31] X.-L. Zhu, M. Chen, S.-M. Weng, P. McKenna, Z.-M. Sheng, and J. Zhang, Single-Cycle Terawatt Twisted-Light Pulses at Midinfrared Wavelengths above 10 μm , *Phys. Rev. Appl.* **12**, 054024 (2019).
- [32] X.-L. Zhu, S.-M. Weng, M. Chen, Z.-M. Sheng, and J. Zhang, Efficient generation of relativistic near-single-cycle mid-infrared pulses in plasmas, *Light: Sci. Appl.* **9**, 46 (2020).
- [33] P. Sprangle, E. Esarey, and A. Ting, Nonlinear Theory of Intense Laser-Plasma Interactions, *Phys. Rev. Lett.* **64**, 2011 (1990).
- [34] T. Tajima and J. M. Dawson, Laser Electron Accelerator, *Phys. Rev. Lett.* **43**, 267 (1979).
- [35] C. Joshi, W. B. Mori, T. Katsouleas, J. M. Dawson, J. M. Kindel, and D. W. Forslund, Ultrahigh gradient particle acceleration by intense laser-driven plasma density waves, *Nature (London)* **311**, 525 (1984).
- [36] P. Mora and T. M. Antonsen, Jr., Electron cavitation and acceleration in the wake of an ultraintense, self-focused laser pulse, *Phys. Rev. E* **53**, R2068 (1996).
- [37] A. Pukhov and J. Meyer-ter-Vehn, Laser wake field acceleration: the highly non-linear broken-wave regime, *Appl. Phys. B* **74**, 355 (2002).
- [38] W. Lu, C. Huang, M. Zhou, W. B. Mori, and T. Katsouleas, Nonlinear Theory for Relativistic Plasma Wakefields in the Blowout Regime, *Phys. Rev. Lett.* **96**, 165002 (2006).
- [39] C. H. Pai, Y. Y. Chang, L. C. Ha, Z. H. Xie, M. W. Lin, J. M. Lin, Y. M. Chen, G. Tsaur, H. H. Chu, S. H. Chen, J. Y. Lin, J. Wang, and S. Y. Chen, Generation of intense ultrashort midinfrared pulses by laser-plasma interaction in the bubble regime, *Phys. Rev. A* **82**, 063804 (2010).
- [40] Z. Nie, C.-H. Pai, J. Zhang, X. Ning, J. Hua, Y. He, Y. Wu, Q. Su, S. Liu, Y. Ma *et al.*, Photon deceleration in plasma wakes generates single-cycle relativistic tunable infrared pulses, *Nat. Commun.* **11**, 2787 (2020).
- [41] X.-L. Zhu, W.-Y. Liu, S.-M. Weng, M. Chen, Z.-M. Sheng, and J. ZhangJie, Generation of single-cycle relativistic infrared pulses at wavelengths above 20 μm from density-tailored plasmas, *Matter Radiat. Extremes* **7**, 014403 (2022).
- [42] Y. Ma, D. Seipt, A. E. Hussein, S. Hakimi, N. F. Beier, S. B. Hansen, J. Hinojosa, A. Maksimchuk, J. Nees, K. Krushelnick, A. G. R. Thomas, and F. Dollar, Polarization-Dependent Self-Injection by Above Threshold Ionization Heating in a Laser Wakefield Accelerator, *Phys. Rev. Lett.* **124**, 114801 (2020).
- [43] M. Vargas, W. Schumaker, Z. H. He, Z. Zhao, K. Behm, V. Chvykov, B. Hou, K. Krushelnick, A. Maksimchuk, V. Yanovsky, and A. G. R. Thomas, Improvements to laser wakefield accelerated electron beam stability, divergence, and energy spread using three-dimensional printed two-stage gas cell targets, *Appl. Phys. Lett.* **104**, 174103 (2014).
- [44] A. E. Hussein, N. Senabulya, Y. Ma, M. J. V. Streeter, B. Kettle, S. J. D. Dann, F. Albert, N. Bourgeois, S. Cipiccia, J. M. Cole, O. Finlay, E. Gerstmayr, I. Gallardo González, A. Higginbotham, D. A. Jaroszynski, K. Falk, K. Krushelnick, N. Lemos, N. C. Lopes, C. Lumsdon, O. Lundh, SPD Mangles *et al.*, Laser-wakefield accelerators for high-resolution x-ray imaging of complex microstructures, *Sci. Rep.* **9**, 3249 (2019).
- [45] R. A. Fonseca, L. O. Silva, F. S. Tsung, V. K. Decyk, W. Lu, C. Ren, W. B. Mori, S. Deng, S. Lee, T. Katsouleas, and J. C. Adam, Osiris: A three-dimensional, fully relativistic particle in cell code for modeling plasma based accelerators, in *International Conference on Computational Science* (Springer, Berlin, 2002), pp. 342–351.
- [46] R. A. Fonseca, S. F. Martins, L. O. Silva, J. W. Tonge, F. S. Tsung, and W. B. Mori, One-to-one direct modeling of experiments and astrophysical scenarios: Pushing the envelope on kinetic plasma simulations, *Plasma Phys. Controlled Fusion* **50**, 124034 (2008).
- [47] Z.-H. He, B. Hou, V. Lebailly, J. A. Nees, K. Krushelnick, and A. G. R. Thomas, Coherent control of plasma dynamics, *Nat. Commun.* **6**, 7156 (2015).
- [48] R. J. Shalloo, S. J. D. Dann, J.-N. Gruse, C. I. D. Underwood, A. F. Antoine, C. Arran, M. Backhouse, C. D. Baird, M. D. Balcazar, N. Bourgeois *et al.*, Automation and control of laser wakefield accelerators using bayesian optimization, *Nat. Commun.* **11**, 6355 (2020).
- [49] M. J. V. Streeter, S. Kneip, M. S. Bloom, R. A. Bendoyro, O. Chekhlov, A. E. Dangor, A. Döpp, C. J. Hooker, J. Holloway, J. Jiang *et al.*, Observation of Laser Power Amplification in a Self-Injecting Laser Wakefield Accelerator, *Phys. Rev. Lett.* **120**, 254801 (2018).
- [50] M. J. V. Streeter, Y. Ma, B. Kettle, S. J. D. Dann, E. Gerstmayr, F. Albert, N. Bourgeois, S. Cipiccia, J. M. Cole, I. Gallardo González *et al.*, Characterization of laser wakefield acceleration efficiency with octave spanning near-IR spectrum measurements, *Phys. Rev. Accel. Beams* **25**, 101302 (2022).
- [51] S. V. Bulanov, F. Pegoraro, A. M. Pukhov, and A. S. Sakharov, Transverse-Wake Wave Breaking, *Phys. Rev. Lett.* **78**, 4205 (1997).
- [52] R. M. G. M. Trines, C. D. Murphy, K. L. Lancaster, O. Chekhlov, P. A. Norreys, R. Bingham, J. T. Mendonca, L. O. Silva, S. P. D. Mangles, C. Kamperidis, A. Thomas, K. Krushelnick, and Z. Najmudin, Photon acceleration and modulational instability during wakefield excitation using long laser pulses, *Plasma Phys. Controlled Fusion* **51**, 024008 (2009).
- [53] B. A. Shadwick, C. B. Schroeder, and E. Esarey, Nonlinear laser energy depletion in laser-plasma accelerators, *Phys. Plasmas* **16**, 056704 (2009).
- [54] S. P. D. Mangles, A. G. R. Thomas, M. C. Kaluza, O. Lundh, F. Lindau, A. Persson, F. S. Tsung, Z. Najmudin, W. B. Mori, C.-G. Wahlström, and K. Krushelnick, Laser-Wakefield Acceleration of Monoenergetic Electron Beams in the First Plasma-Wave Period, *Phys. Rev. Lett.* **96**, 215001 (2006).
- [55] E. N. Nerush and I. Yu. Kostyukov, Carrier-Envelope Phase Effects in Plasma-Based Electron Acceleration with Few-Cycle Laser Pulses, *Phys. Rev. Lett.* **103**, 035001 (2009).
- [56] P. E. Masson-Laborde, M. Z. Mo, A. Ali, S. Fourmaux, P. Lassonde, J. C. Kieffer, W. Rozmus, D. Teychenné, and R. Fedosejevs, Giga-electronvolt electrons due to a transition from laser wakefield acceleration to plasma wakefield acceleration, *Phys. Plasmas* **21**, 123113 (2014).
- [57] W. P. Leemans, B. Nagler, A. J. Gonsalves, Cs. Tóth, K. Nakamura, C. G. R. Geddes, E. Esarey, C. B. Schroeder, and S. M. Hooker, GeV electron beams from a centimetre-scale accelerator, *Nat. Phys.* **2**, 696 (2006).
- [58] S. Kneip, S. R. Nagel, S. F. Martins, S. P. D. Mangles, C. Bellei, O. Chekhlov, R. J. Clarke, N. Delerue, E. J. Divall, G. Doucas *et al.*, Near-GeV Acceleration of Electrons by a Nonlinear

- Plasma Wave Driven by a Self-Guided Laser Pulse, *Phys. Rev. Lett.* **103**, 035002 (2009).
- [59] S. Kneip, C. McGuffey, J. L. Martins, S. F. Martins, C. Bellei, V. Chvykov, F. Dollar, R. Fonseca, C. Huntington, G. Kalintchenko, A. Maksimchuk, S. P. D. Mangles, T. Matsuoka, S. R. Nagel, C. A. J. Palmer, J. Schreiber, K. T. Phuoc, A. G. R. Thomas, V. Yanovsky, L. O. Silva *et al.*, Bright spatially coherent synchrotron X-rays from a table-top source, *Nat. Phys.* **6**, 980 (2010).
- [60] B. Kettle, E. Gerstmayr, M. J. V. Streeter, F. Albert, R. A. Baggott, N. Bourgeois, J. M. Cole, S. Dann, K. Falk, I. Gallardo González *et al.*, Single-Shot Multi-keV X-Ray Absorption Spectroscopy Using an Ultrashort Laser-Wakefield Accelerator Source, *Phys. Rev. Lett.* **123**, 254801 (2019).